41st AIAA/ASME/SAE/ASEE Joint Propulsion Conference and Exhibit
July 10–13, 2005/Tucson, AZ

# A LES - PIV investigation of a Stagnation Point Reverse Flow Combustor

V. Sankaran*
P. Gopalakrishnan†, S. Undapalli‡
V. Parisi§, J. Seitzman¶& S. Menon‖
*School of Aerospace Engineering*
*Georgia Institute of Technology*
*Atlanta, Georgia 30332*

**The demand for less polluting combustion devices and processes are ever increasing because of the legislative regulations and environmental concerns. On the other hand, the depleting oil resources demands high efficiency combustion. The requirement of low emissions in conjunction with high efficiency represents a conflict of interest and pose serious challenge for combustion researchers and combustor designers. A lab-scale burner referred to as Stagnation Point Reverse Flow (SPRF) combustor, has been built in Georgia Tech., which incorporates a novel design to achieve exhaust-gas recirculation, premixing and dilution. In this study, a combined numerical and experimental technique has been used to explore the flow and flame structure in the SPRF combustor. Results are reported from three simulations: a non-reactive flow in the premixed mode, a reactive flow in the premixed mode and a non-reactive flow in the non-premixed mode. Non-reactive premixed LES has been compared with the corresponding PIV data. Increased entrainment, higher turbulent intensities, pronounced exhaust gas recirculation, distributed reaction zone and smooth thermal gradients were observed in the reactive flow simulation.**

## I. Introduction

The demand for low emissions along with more energy efficient combustion systems has been a major driving force to develop innovative combustion technologies. In conventional burners and combustors, air preheating and/or higher operating pressure ratios are employed to enhance the thermal efficiency. A negative consequence of this approach is the increase in peak flame temperatures and augmented pollutant emissions. Some alternate concepts in use for reducing the peak flame temperatures are staged combustion, catalytic combustion, lean-premixed combustion, and exhaust gas recirculation in the flames. Even though, these alternate approaches reduce emissions, often it also gives rise to issues regarding flame stability, flame

*Post Doctoral Fellow, AIAA Member
†Graduate Research Assistant
‡Graduate Research Assistant, AIAA Student Member
§Graduate Research Assistant
¶Professor, AIAA Associate Fellow
‖Professor, AIAA Associate Fellow

Copyright © 2005 by Sankaran, Gopalakrishnan, Undapalli, Parisi, Seitzman and Menon. Published by the American Institute of Aeronautics and Astronautics, Inc. with permission.

noise and safety. Recently, a new combustion process/phenomena referred to as mild/dilute combustion or high temperature-air combustion or flameless oxidation has been identified that meets the conflicting requirements of high thermal efficiency and low emissions without introducing additional problems related to flame stability. In this set-up, the exhaust gases are mixed with the combustion air and/or fuel prior to the chemical reaction. It should be noted that, in such a set-up, the exhaust gases not only preheat the air needed for combustion, but also dilutes the reactant mixture, thereby reducing the overall flame temperature and emission of harmful gases.

The physics behind this phenomena can be explained as follows. Formation rate of thermal NOx depends on the local temperature and the oxygen concentration in a combustor. At temperatures greater than 1500 K, even a short residence time results in high NOx emissions, because of the exponential dependence of the NOx formation rate on temperature. By diluting the fuel-air mixture with the flue gas, oxygen concentration is lowered, and hence, the reaction rates are also lowered. Consequently, combustion is no longer confined to a thin front, instead a volumetric reaction zone that is spread over the entire mixing region is realized.[1] The weak/low reaction rates results in the smooth variation of thermal gradients, and hence reducing pollutants emissions without compromising thermal efficiency.

The characteristics of the flame in this mode of combustion depend on fuel property, preheat air temperature, oxygen concentration in air, and most importantly, the geometry of the combustor.[2] Some of the characteristics are, no visible flame structure, no/low sound emission,[1] and ultra low emission of pollutants. In addition to low emission levels, this mode of combustion has further advantages over other NOx reduction techniques in terms of safety and reliability. Moreover, relatively uniform wall temperatures can be obtained in this mode of combustion which reduces the thermal stresses on the mechanical parts and hence increases mean time between failures of the gas turbine components. Another interesting feature of this combustion mode is that the flame structure is strongly related to the mixing process and flow patterns in the entire combustor. In contrast, the normal mode of combustion is highly sensitive to mixing and flame holding in the near field of the nozzle[2]

As a result of all these desirable features there is a a great deal of interest in this technology. For instance, Wunning and Wunning[1] investigated a FLOX burner employing a direct fuel and oxidizer injection and identified a set of operating conditions with NOx emissions ranging from 6 to 100 ppm @ 3 % $O_2$ for which no visible flame was observed. Hence, this mode of combustion is called the flameless combustion. The studies of Katsuki *et al*[3] and and Sato[4] also demonstrated similar characteristics of combustion using high temperature air. The resulting flames had a uniform temperature field and low levels of temperature fluctuation with low pollutant emissions. Fujimori et al.[5] performed experiments with high speed lifted jet flames and showed that the presence of lifted flame improves the dilution of the fuel-air mixture that leads to slow reaction and low NOx emissions. The lifted flames were also shown to suppress the formation of a thin, intense reaction zone thus ensuring a broader reaction zones with uniform temperatures.

Despite the fact that the feasibility of this technology has been demonstrated in full-scale plants, there is still a considerable lack of knowledge on the basic phenomena, as well as the real advantages and problems related to the switch from the diffusion controlled regime to kinetic-controlled one. Increasingly, combustor designers for aircrafts are also turning their attention towards developing cleaner and quieter combustors based on flameless/mild combustion, due to the stringent requirements on emission and noise levels for the current aircrafts. This would involve developing combustors that can operate in both normal mode (for cold start and high power operations) and in mild/flameless combustion mode. All these reasons warrant further efforts to understand the basic mechanisms in mild/flameless combustion and the impact of the parameters that affect this mode of combustion. But unfortunately, most of the earlier work has been directed towards developing large volume industrial burners. However, the fundamentals of this technology can be investigated using well-controlled conditions achieved in a laboratory scale burner.

Consequently, a lab-scale burner referred to as Stagnation Point Reverse Flow (SPRF) combustor, has been built in Georgia Tech., which incorporates a novel design to achieve exhaust-gas recirculation, premixing and dilution. Moreover, this ingenious design also allows it to operate in premixed or non-premixed mode with a great flexibility to vary parameters at ease. Therefore, the main goal of this work is to investigate

using a combined numerical(LES) and experimental (PIV) approach (1) to understand the fundamental mixing processes in this combustor, (2) to characterize the salient features of mixing and combustion,and (3) to study the effects of preheating and dilution on the flow-mixing patterns, flame structure and emissions.

## II. Experimental Set-Up

The schematic diagram of the SPRF combustor is shown in figure 1(a) The experimental apparatus consists of three major components: a combustor, an injector and an air/fuel supply system. The combustor is a cylindrical quartz tube (4) wrapped with thermal insulation and closed on one side with an end plate (6) (stagnation end). The injector is located at the open end of the tube (opposite to the end plate) with its axis coinciding with the axis of the cylindrical quartz tube. The injector consists of concentric tubes to discharge the fresh mixture into the combustor. In the non-premixed mode, fuel flows from the central tube (2) and the air flows from the concentric annular tube (3) surrounding it. The same combustor can also be operated in the premixed mode by simply shutting off the fuel supply (1) flowing through the central tube, and by discharging the fuel-air mixture through the annular tube into the combustor.[6]

Fresh reactant mixture enters the combustor from the tip of the injector. As the flow reaches the stagnation end of the combustor, it turns back and flow towards the open end of the combustor to leave the system. During this reverse flow, some of the exhaust gases are entrained back into the combustor by the high velocity reactant stream from the injector. The exhaust gases, as they flow over the walls of the injector also preheats the reactants flowing inside the injector. Note, this simple design is extremely flexible to perform a whole range of parametric studies. By varying the penetration depth of the injector into combustor, the amount of preheating can be altered. By varying the incoming mixture velocity, the amount of entrainment, and hence the amount of exhaust gas dilution can be varied.

Two factors are important for achieving high thermal efficiency and low emissions: premixing of the reactant mixture (fuel, air or both) with the exhaust gases and high internal turbulence. The first allows dilution of the reactants and increases the characteristic time of the reactions involved; the second reduces the mixing time. The overall effect is to obtain Damkohler number as small as possible.[7] The SPRF combustor promotes both of these favorable conditions. The current combustor (SPRFC) also stands apart from most of the existing mild/flameless combustors by two main characteristics: (1) The working volume for the combustion process is much smaller than those found in industrial combustors. This feature meets aircraft requirements for small volumes and high power-weight ratios. (2) The incoming reactants are preheated by the exhaust flow: in other flameless burners the external air is preheated using external devices (e.g. heaters, heat exchangers, etc.) while this combustor may be defined as self-contained

### A. PIV-Setup

In contrast to conventional measurement techniques, which provide single point measurements, PIV is a non-intrusive technique that can be used to obtain instantaneous whole field measurements of flows. PIV technique is also a more direct measure of the velocity of a fluid since it depends directly on the displacement of the tracer particle during a given time period. The PIV set-up is made up of three major parts - a source of illumination, a seeder which generates the tracer particles required for the measurements and an interline CCD camera for image acquisition. The combustor essentially consists of a quartz tube 70 $mm$ in diameter, with a quartz end plate. The light sheet was produced using the second harmonic green light at 532 $nm$ produced by a dual head pulsed ND-YAG laser. Each laser head is capable of providing light pulses with 150 $mJ$ of energy at the rate of 10 $Hz$. Since the laser pulse is very short (FWHM of 8ns) it effectively freezes the flow even up to supersonic velocities. The beam is then converted into a thin sheet of appropriate width using a set of three cylindrical lenses. The seed particles are generated using a fluidized bed particle generator with an air turbine vibrator. The seed material used was $0.3 - 0.5m$ alumina particles that were baked before-hand to prevent particle agglomeration. The illuminated particles are imaged using a 12 bit MicroMAX Interline CCD camera from Roper-Scientific. The full chip resolution of the camera is 1300 X

1030 pixels and it is equipped with a 50 $mm$ Nikkor lens (f: 1/1.8) for image capture. The pulse separation between the two laser pulses and the camera frames is controlled by using a delay generator (Stanford, DG535).

The first set of experiments was conducted in non-reacting flow with air flowing through the outer section of a co-annular injector at atmospheric pressure and temperature. Air is first sent through the seeder where alumina particles are picked up. The seeded air then exits into the combustor through the injector. For the pre-mixed reacting flow case, natural gas is mixed with the seeded air before it exits into the combustor. A one-inch thick alumina tube is used to insulate the combustor thereby keeping the heat losses low.

A gas analyzer probe is located near the outflow is used to measure the emissions (CO and NO) from the combustor. Reactant and product temperature are measured by two thermo-couples located inside the combustor. Both internal and external temperature are also measured.

## III. Governing Equations

The conservation equations of mass momentum, energy and species equations for LES are given by:

$$
\begin{array}{ll}
\frac{\partial \bar{\rho}}{\partial t} & + \frac{\partial \bar{\rho}\tilde{u}_i}{\partial x_i} = 0 \\
\frac{\partial \bar{\rho}\tilde{u}_i}{\partial t} & + \frac{\partial}{\partial x_j}[\bar{\rho}\tilde{u}_i\tilde{u}_j + \bar{p}\delta_{ij} - \bar{\tau}_{ij} + \tau_{ij}^{sgs}] = 0 \\
\frac{\partial \bar{\rho}\tilde{E}}{\partial t} & + \frac{\partial}{\partial x_i}[(\bar{\rho}\tilde{E} + \bar{p})\tilde{u}_i + \bar{q}_i - \tilde{u}_j\bar{\tau}_{ji} + H_i^{sgs} + \sigma_i^{sgs}] = 0 \\
\frac{\partial \bar{\rho}\tilde{Y}_k}{\partial t} & + \frac{\partial}{\partial x_i}[\bar{\rho}\tilde{Y}_k\tilde{u}_i - \bar{\rho}\tilde{Y}_k\widetilde{V_{i,k}} + Y_{i,k}^{sgs} + \theta_{i,k}^{sgs}] = \bar{\dot{w}}_k
\end{array}
$$

where $k = 1$ to $N_s$ and $N_s$ is the total number of species present in the system. $\bar{q}_i$ is the heat flux vector given by: $\bar{q}_i = -\bar{\kappa}\frac{\partial \tilde{T}}{\partial x_i} + \bar{\rho}\sum_{k=1}^{N_s}\tilde{h}_k\tilde{Y}_k\widetilde{V_{i,k}} + \sum_{k=1}^{N_s} q_{i,k}^{sgs}$ The diffusion velocities are approximated using Fickian diffusion as $\widetilde{V_{i,k}} = (-\bar{D}_k/\tilde{Y}_k)(\partial\tilde{Y}_k/\partial x_i)$. The subgrid terms that require closure are:

$$
\begin{array}{rcl}
\tau_{ij}^{sgs} & = & \overline{\rho}\,(\widetilde{u_i u_j} - \widetilde{u}_i\widetilde{u}_j) \\
H_i^{sgs} & = & \overline{\rho}\,(\widetilde{Eu_i} - \widetilde{E}\widetilde{u}_i) + (\overline{pu_i} - \overline{p}\widetilde{u}_i) \\
\sigma_i^{sgs} & = & \widetilde{u_j\tau_{ij}} - \widetilde{u}_j\overline{\tau}_{ij}. \\
Y_{i,k}^{sgs} & = & \bar{\rho}[\widetilde{u_i Y_k} - \tilde{u}_i\tilde{Y}_k] \\
q_{i,k}^{sgs} & = & [\overline{h_k D_k \partial Y_k/\partial x_i} - \tilde{h}_k\tilde{D}_k\partial\tilde{Y}_k/\partial x_i] \\
\theta_{i,k}^{sgs} & = & \bar{\rho}[\widetilde{V_{i,k}Y_k} - \widetilde{V}_{i,k}\widetilde{Y}_k]
\end{array}
\tag{1}
$$

The pressure is determined from the filtered equation of state, $\bar{p} = \bar{\rho}R\tilde{T} + T^{sgs}$. Here, $T^{sgs}$ is the temperature-species correlation term, defined as $[\widetilde{Y_k T} - \tilde{Y}_k\tilde{T}]$. For low heat-release, $T^{sgs}$ can be expected to be negligible[8] but this may not be true for high heat release. However, due to the difficulty in modeling these terms they are generally neglected.[8,9] The filtered total energy per unit volume is given by $\bar{\rho}\tilde{E} = \bar{\rho}\tilde{e} + \frac{1}{2}\bar{\rho}\tilde{u}_i\tilde{u}_i + \bar{\rho}k^{sgs}$ where, the subgrid kinetic energy (to be discussed later) is defined as, $k^{sgs} = (1/2)[\widetilde{u_k u_k} - \tilde{u}_k\tilde{u}_k]$. The filtered internal energy for calorically perfect gases is given by $\tilde{e} = \sum_{k=1}^{N_s}[c_{v,k}\tilde{Y}_k\tilde{T} + \tilde{Y}_k$ where, $\Delta h'_{f,k} = \Delta h^0_{f,k} - c_{p,k}T^0$ and $\Delta h^0_{f,k}$ is the standard heat of formation at a reference temperature $T^0$.

The subgrid stress tensor $\tau_{ij}^{sgs}$ is modeled as $\tau_{ij}^{sgs} = -2\rho\nu_t[\tilde{S_{ij}} - \frac{1}{3}\tilde{S_{kk}}\delta_{ij}] + \frac{2}{3}\bar{\rho}k^{sgs}\delta_{ij}$. To complete the closure for the subgrid stresses, the subgrid eddy viscosity $\nu_t$ and the subgrid kinetic energy, $k^{sgs}$ need to be modeled. A non-equilibrium model[10,11] using a transport equation for the subgrid kinetic energy, $k^{sgs}$ is used in this study and is given by :

$$
\frac{\partial\overline{\rho}k^{sgs}}{\partial t} + \frac{\partial}{\partial x_i}(\overline{\rho}\tilde{u}_i k^{sgs}) = \frac{\partial}{\partial x_i}\left(\overline{\rho}\frac{\nu_t}{Pr_t}\frac{\partial k^{sgs}}{\partial x_i}\right) + P^{sgs} - \epsilon^{sgs}
$$

The terms, $P^{sgs}$ and $\epsilon^{sgs}$ in the above equation are respectively, production and dissipation of subgrid kinetic energy. The subgrid dissipation, $\epsilon^{sgs}$ is obtained by integrating the dissipation spectrum ($D(k) = -2\nu k^2 E(k)$) over the unresolved wavenumbers,[12] to get $\epsilon^{sgs} = C_\epsilon \rho (k^{sgs})^{3/2}/\overline{\Delta}$ where, $C_\epsilon = 0.916$. The subgrid production term is modeled as $P^{sgs} = -\tau_{ij}^{sgs}(\partial \widetilde{u}_i/\partial x_j)$. The coefficient $Pr_t$ is the turbulent Prandtl number and is taken to be 0.9. The subgrid eddy viscosity is modeled as[12] $\nu_t = C_\nu \sqrt{k^{sgs}}\Delta$, where $C_\nu = 0.067$ nominally. However, both $C_\nu$ and $C_\epsilon$ can be obtained as a part of the solution by using the dynamical procedure, as shown earlier.[13]

In addition to $\tau_{ij}^{sgs}$, several unclosed terms appear in the LES filtered energy and species equations given in Eqn. (1), such as: $H_i^{sgs}$: subgrid enthalpy flux; $\sigma_i^{sgs}$: subgrid viscous work; $Y_{i,k}^{sgs}$: convective species flux; $q_{i,k}^{sgs}$: subgrid heat flux; $\theta_{i,k}^{sgs}$:subgrid species diffusive flux; The subgrid total enthalpy flux $H_i^{sgs}$ is modeled using the eddy viscosity model as follows: $H_i^{sgs} = (-\overline{\rho}\nu_t/Pr_t)(\partial \tilde{H}_k/\partial x_i)$. Note that, since large-scale motion is resolved in LES, the associated counter-gradient processes in the resolved scales are also resolved (even though a gradient closure is employed for $H_i^{sgs}$).

A conventional gradient diffusion model is employed for the the subgrid scalar transport closure. In this gradient diffusion closure, the subgrid convective species flux $Y_{i,k}^{sgs}$, given in equation Eqn. [1] is modeled as follows: $Y_{i,k}^{sgs} = (-\overline{\rho}\nu_t/Sc_t)(\partial \tilde{Y}_k/\partial x_i)$ The coefficient $Sc_t$ is the turbulent Schmidt Number, and is taken to be unity. It should be noted that earlier, theory and experiments[14] have shown that this type of gradient diffusion closure for species transport can lead to significant errors, especially when used in the time-averaged RANS context. Nevertheless, since the large-scale motion is resolved in a LES, the limitation of a subgrid eddy diffusivity closure is not that apparent, unless counter-gradient effects occur at the grid scale. Therefore, using this model as a baseline subgrid closure for LES is acceptable as a first approximation.

The other unclosed terms, $\sigma_i^{sgs}$, $q_{i,k}^{sgs}$ and $\theta_{i,k}^{sgs}$, are often neglected in the conventional closure approach, and there exists no model for these terms.[15] These terms are the subgrid contribution of the molecular diffusive flux and are often neglected assuming that their contributions are small in high Reynolds number flows.[8,9]

## IV. Numerical Method and Boundary Conditions

The governing filtered unsteady compressible Navier-Stokes equations are discretized in time and space and solved using a finite-volume formulation in generalized co-ordinates. The numerical scheme is second-order accurate in space and time. The computational domain is resolved using $90 \times 75 \times 51$ grid points along, the axial, the radial, and the azimuthal directions, respectively. A non-uniform grid that is clustered near regions of high gradients is employed in the present study. The grid resolution used here provides a $y^+ = 15$ near the walls of the injector. The axial grid is clustered around the point of jet expansion. It is then stretched after one diameter of the jet which is clustered again near the stagnation end of the combustor. Inflow and outflow boundary conditions were set using the characteristic conditions of Poinsot and Lele.[16] On all solid walls, no-slip conditions were prescribed for the velocity field. Adiabatic and non-catalytic wall boundary conditions were used for the temperature and the species field.

The present LES study was designed to match the PIV measurements performed in the same configuration. For the non-reacting case, a jet of air at atmospheric pressure and temperature flows into the combustor at a volumetric flow rate of $0.00578 m^3/s$. This value is matched in the simulations using a fully developed turbulent inlet velocity profile with a peak velocity of $72 m/s$. An RMS velocity profile with 5 % intensity has been superimposed on this mean velocity profile.

In the current study, an Eddy-Break-Up model[17] (EBU) is used as the subgrid combustion model. This model attempts to include the sub-grid mixing effects on the assumption that, the combustion process can be assumed to be either kinetics controlled or mixing controlled (depending the relative time-scales between them). As a result, at any instant the reaction rate is computed as the minimum of the kinetic reaction rate and the mixing rate. This is explained as follows

For a general reaction mechanism comprising of $N_r$ reactions given by $\sum_{k=1}^{N_s} \nu'_{k,j} M_{k,j} \rightleftharpoons \sum_{k=1}^{N_s} \nu"_{k,j} M_{k,j}$

the filtered reaction rates for species "k" is computed as follows $\bar{\dot{w}}_k = W_k \sum_{j=1}^{N_r} (\nu"_{k,j} - \nu'_{k,j}) \min[q_j^{mix}, q_j^{kin}]$ where $q_j^{mix}$ and $q_j^{kin}$ are the molar reaction rates based on mixing and Arrhenius chemical kinetic rate, respectively. The Arrhenius reaction rates for step "j" is given by, $q_j^{kin} = k_{f,j} \prod_{k=1}^{N_s} [M_k]_{k,j}^{\nu"} - k_{b,j} \prod_{k=1}^{N_s} [M_k]_{k,j}^{\nu'}$ and the mixing rates for the forward and the backward reactions are given by

$$q_{j,f}^{mix} = \frac{1}{\tau_M} \min\left(\frac{[M_k]}{\nu"_{k,j}}\right) \qquad \text{and} \qquad q_{j,b}^{mix} = \frac{1}{\tau_M} \min\left(\frac{[M_k]}{\nu'_{k,j}}\right) \tag{2}$$

Here, $\tau_M$ is the mixing time scale and is related to the sub-grid turbulence as follows $\tau_M = C_{EDC} \frac{\overline{\Delta}}{\sqrt{k^{sgs}}}$

The most severe draw-back of this approach is the use of heuristic non-universal calibration constants. This description of the chemical reaction in turbulent flows is too simple to yield any reasonably good predictions, even though it is computationally cheap. Future studies will revisit this case using the LEMLES approach that has the ability to predict turbulent-chemistry interactions more accurately.

## V. Results and Discussion

Results obtained from the LES and PIV of the stagnation point reverse flow combustor is reported here. Three cases have been investigated: A non-reactive flow in the premixed mode, a reactive flow in the premixed mode and a non-reactive flow in the non-premixed mode. Non-reactive premixed LES has been compared with the corresponding PIV data. Statistically averaged results are provided for both the non-reacting and the reacting cases.

### A. Non-Reactive jet - premixed mode

The flow configuration is shown in Fig. 1(a) It consists of an annular jet of air flowing from the injector into the combustor. In the experiments, the central tube was shut-off upstream to prevent any flow from the central tube. This creates a cylindrical cavity, into which the fluid from the combustor can flow in. To accurately simulate the flow conditions, this cylindrical cavity is included in the computations. But to reduce the computational cost, the length of the cylindrical cavity is restricted to be equal to the length of the injector.

Figure 1(b) shows the variation of the mean axial velocity along the center-line of the combustor. As the annular jet leaves the injector, it is slowed down by the presence of cylindrical cavity. This causes a small recirculation bubble at the tip of the injector, near the center tube. As the fluid continues to flow, the shear layers merge and accelerates the flow to a peak velocity as high as the bulk velocity of the jet ($67m/s$) in the annular pipe. Even though the location of the peak agrees well between LES and PIV, the computation slightly under-predicts this peak velocity. The source of this error could be attributed to both LES (coarse grid) and experiments (more samples, better PIV resolution). The reason is not clear at this time. Beyond this location, the axial velocity begins to decrease rapidly until it reaches the stagnation end of the combustor. In approximately 2/3 rd of the length of the combustor, the center-line velocity falls down to 2 % of the initial bulk velocity. This center-line velocity decay is in better agreement with the measurements. The significance of this stagnation zone and its implication on combustion will be discussed in the next section.

Figures 2(a) and (b) show the mean axial velocity profiles at 8 axial locations in the combustor, respectively. The comparison of LES results with PIV data is also shown in the figure. The agreement between the LES and PIV are reasonable. The computations exhibit more symmetry than the measurements. Both LES and PIV shows the strong entrainment of the reverse flow gases into the jet. This causes a rapid growth of the mixing layer which saturates after approximately half the length of the combustor. After this point, the flow around the center-line of the combustor feels presence of the stagnation region and slows down rapidly, resulting in a more uniform velocity profile near the stagnation end of the combustor.

Figures 3(a) and (b) show the comparison of RMS axial velocity profiles at 8 axial locations in the combustor. Note, that LES only gives the resolved part of the turbulence intensities. The agreement

between PIV and LES are satisfactory near the injector and gets better downstream. Even though the trend and the locations of the peak are predicted reasonably well, PIV shows a much larger scatter in the near field and more asymmetry leading one to believe that source of the error comes from the experiments. The peak in the turbulent intensity occurs at the shear layers, where the turbulent production is high, due to the counter-flowing streams of the incoming air and the outgoing gases. The counter-flow arrangement results in a peak turbulent intensity that is approximately 25 % of the bulk inflow velocity (at X = 31 mm). Note, this is a favorable condition for entraining the outflowing exhaust gases into the fresh mixture. As the fluid flows downstream, the peaks move closer to the center-line and finally most of the turbulence subsides at the closed end of the tube. From the combustion point of view, this means that the burning process is no longer governed by the turbulent mixing but purely determined by the chemical time scales in these regions.

Figure 4(a) shows the variation of RMS of the axial velocity along the center line of the combustor. As it can be observed, the RMS velocity increases at the tip of the injector (X = 10 mm from the injector), due to the presence of the recirculation bubble and then decrease for a small distance until the shear layers merge, following which the turbulence increases (around X = 31 mm). This is then followed by a continuous decay of the turbulence till the stagnation zone of the combustor. It should be noted that the turbulence decays to near zero values at the stagnation end of the combustor, indicating that the turbulent mixing is not an important factor in the stagnation zone of the combustor.

The location and structure of the stagnation zone plays an important role in combustion process. Figure 4(b) shows the contours of zero-axial-velocity as obtained from the LES and PIV measurements. Note that the injector is located on the right side of the combustor and the closed end of the tube is on the left. In this figure, all regions in blue mark the fluid flowing from left to right and the regions in red mark the fluid flowing from right to left. The region where the color changes from red to blue are regions of zero velocity. Once again, the agreement between LES and PIV are reasonable. As it can be noted, both LES and PIV show that the stagnation zone is situated approximately 50 mm from the closed end of the combustor (on the left). The presence of this stagnation zone plays a significant role during combustion. The unburnt / partially burnt reactants that reach the closed end of the tube are trapped in the stagnation zone with hot burnt products. This increases the residence time for the slow reacting pollutant species such as CO, and thus help in oxidizing them to less harmful gases.

Figures 5(a) and (b) show the contours of mean axial velocity and the streamlines pattern in the combustor, respectively. The presence of two large counter-rotating vortices located just below shear layers is evident in these figures. These flow structures account for the interaction between inflow jet and reverse flow and the entrainment process. The flow features are symmetric indicating the statistical stationarity of the first two moments of the flow-field. The formation of the tip recirculation bubble at the injector is also apparent in the contours of mean velocity. The streamlines plot (fig. 5(b)) also indicate the formation of a toroidal-recirculation region at the stagnation end of the tube. The reverse flow from the closed end of the tube to the open end is entrained by the high velocity jet, as indicated by the converging streamlines pattern near the tip of the injector. Figure 5(c) shows that the turbulent mixing is very effective only in the mid-section of the combustor. This indicates that the exhaust gases entrained back near the tip of the injector is mixed thoroughly with the fresh mixture near the center of the combustor. It is expected that in this region, the turbulent mixing times and chemical times are of the same order (Damkohler number$\approx$1) hence reaching conditions of a perfectly stirred reactor. On the other hand, turbulent mixing is highly confined to the shear layer near the injector and it is least effective near the stagnation zone of the combustor.

### B. Reactive jet - premixed mode

Results obtained from the reactive LES of the SPRF combustor with an eddy-break-up model are presented here. The flow conditions used for the reactive calculations are chosen to match the non-reactive simulations to facilitate easy comparison. The equivalence ratio, $\phi = 0.58$ is used here. It was observed in the experiments that, as the incoming mixture flows through the injector, it is preheated to 500 K (1 atm.) before reaching the tip of the injector. Similar inflow conditions were set in the computations. To maintain the same mass

flow-rate at the preheated temperature, the inflow velocity at the injector tip accelerates to 127 m/s. The combustion-chemistry model uses a four step eight species reduced mechanism.[18] This mechanism includes the following species: $CH_4, O_2, H_2, H, CO, CO_2, H_20, N_2$. $NO_x$ species is not present in this mechanism and hence, is not included in the present study. The authors are aware of the limitations of the EBU combustion model employed here. This preliminary study is only used to understand the flame-structure and the turbulence-chemistry interaction present in the combustor and not meant to predict emission characteristics of the combustor.

Figures 6(a) and (b) compares the mean axial velocity at 8 locations in the combustor, with the corresponding velocity obtained from the non-reactive simulations. It can be observed that the reactive flow velocities are substantially higher than the non-reactive case. Correspondingly the entrainment/reverse flow velocities have also increased (more than twice the velocities encountered in the cold flow). It is interesting to note that, the velocity profile becomes uniform around the same location (50 mm from the closed end) as in the non-reactive case even though the absolute value is not the same.

Figures 7(a) and (b) compares the RMS of the axial velocity at 8 locations in the combustor, with the corresponding velocity obtained from the non-reactive simulations. Higher turbulent intensities are observed in the forward flow and in the reverse flow regions of the combustor. Even at the last section shown (X = 245 mm), significantly high levels of turbulence can be observed. This indicates that the significant turbulent activity present in the stagnation zone may reduce the residence time of the slow-reacting species.

Figure 8(a) shows the contours of mean axial velocity. It can be noticed that the width of the shear layer is lowered compared to the non-reactive case, for a length of 125 mm from the tip of the injector. Beyond this point, the width remains same as that of the non-reactive flow. As a result, the width of the entrainment zone near the injector tip increases in the reactive case. This increases the recycle factor,[1] defined as the ratio of the reverse-flow rate to the inlet jet flow rate. In other words, this implies that the hot jet entrains more of the exhaust gases, thus creating a more favorable condition for reactant dilution thus reducing pollution.

Figure 8(b) shows the contours of the RMS of the axial velocity. It can be noticed that the maximum turbulent intensity has increased twice that of the non-reactive flows. The thickness of the shear layer characterized by vorticity-thickness has also increased correspondingly. Turbulent intensity is finite and non-zero even near the stagnation zone of the combustor, as opposed to the near-zero values found in the non-reactive case. Even though this implies augmented mixing due to both turbulent and molecular processes in the stagnation zone, it also reduces the residence time of the species. This implies that the pollutant species might not be oxidized completely in the stagnation zone, instead, the reaction may be completed as it travels outwards toward the exhaust.

Figure 8(c) shows the contours of mean temperature. Even though the temperature contours exhibit similarities with the conventional burner stabilized flames near the tip of the injector, the flame structure is quite different near the central zone of the combustor. Increased entrainment present in the reactive flow, dilutes the fresh mixture quickly (within 2 annular jet diameters) and reduces the reaction rate considerably. This results in a distributed reaction zone, where the thermal gradients are weak. Thus, the counter-flow arrangement of the incoming reactants and the outgoing exhaust gases as realized in the SPRF combustor, produces a favorable condition for preheating/exhaust gas dilution due to high internal turbulence, and thus, reducing pollutant emissions.

Figure 8(d) shows the contours of mean mass fraction of $CO$ species. $CO$ is one of the major pollutant species found in combustion of hydrocarbon fuels. Usually, $CO$ requires a long residence time to completely oxidize to $CO_2$. CO is primarily formed from the fuel (methane) during the fuel-break-up reaction and is subsequently oxidized through the reaction: $CO + OH = CO_2 + H$.[18] The above reaction strongly depends on the rate of equilibration of H radicals. This is one of the bottlenecks in the hydrocarbon combustion that determines the rate of thermal energy release.[18] As a result, the CO oxidation rate is primarily decided by the chemical kinetics (long residence time and radical equilibration) rather than the turbulent mixing. However, in the EBU model, the rate determining process is defined as the slowest of the mixing-rate (as determined by the $k_{sgs}$) and the chemical rate (as determined by the Arrhenius rate). Even though the turbulence intensity is non-zero at the stagnation zone, $k_{sgs}$ is still very low, and hence, the mixing rate is

the slowest. As a result, the EBU model tends to over-predict the pollutant concentration since it computes the reaction rate based on the rate of mixing.

It can be noticed that the large concentration of $CO$ is formed near the shear layer, where the fuel break-up reaction takes place. This CO is then partially carried to the stagnation zone and the rest of them is entrained back into fresh mixture by the recirculation zone. The turbulence in the shear layers near injector is high, and hence, the mixing rate is of the order of chemical rates there. As a result, the reaction rate predicted by the EBU is more realistic here. As the fluid moves downstream, the turbulence levels drop down, the mixing rate reduces, hence resulting in the under-prediction of the reaction rate and over-prediction of CO concentration. As mentioned earlier, the intention of reactive flow simulation is to investigate the flame structure and mixing characteristics and hence the pollutant characteristics exhibited by this simulation do not represent the typical combustion performance of the SPRF combustor. In fact, the performance of the SPRF combustor in terms of the pollutant emissions is extremely good with CO emissions less than 10 ppm observed in the experiments.[6]

### C. Non-premixed mode - Scalar Mixing

Non-premixed combustion is of great significance to industrial burners and aircrafts because of the safety issues in premixed combustion. To analyze the performance of this combustor in the non-premixed mode, a non-premixed simulation is carried out to study scalar mixing in the same configuration. The conditions such as flow rates and the global equivalence ratios ($\phi = 0.58$) were chosen identically to compare the mixing characteristics and flow structures between the premixed and non-premixed mode. In this set-up, gaseous methane is injected from the central tube at a peak velocity of 33 m/s and the air flows from the annular tube at a peak velocity of 67 m/s. Both fuel and air are at room temperature and pressure. The computational grid uses the same number of grid points as the premixed combustion, except that the grid clustering was altered so as to resolve the shear layer at the fuel/air and the air/exhaust gas interface.

Figures 9(a) and (b) show the contours of mean and RMS of the axial velocity, respectively. The contours look very similar to the premixed mode, qualitatively. The low velocity fuel jet entrains the high velocity air jet and causes a small recirculation bubble (which extends for $7mm$) close to the tip of the injector. This is followed by a region of acceleration (till $40mm$) due to the merging of shear layer from the annular jet, which increases the center-line velocities up to 50 m/s. This region is clearly characterized by strong mixing between the fuel and the air. It is interesting to note that at any radial location before the merging of the fuel and air jet, there exists a pair of counter-rotating eddy structure, one between the air jet and the outflowing gases, and another between the high-speed air jet and the low-speed fuel jet. This is then followed by a gradual decrease in the jet velocity until it reaches the closed end of the tube. As opposed to the premixed case, here, the jet velocity remains non-zero for a much longer distance than the premixed case. The strong entrainment of the outflowing gases by the air-jet is also apparent in the contours of the mean axial velocity.

Figure 9(b) shows that turbulent mixing is more violent in the non-premixed case than the premixed case. This is mainly due to the presence of multiple shear layers which increase the production of the turbulent kinetic energy. Turbulent mixing is very effective in the central zone of the combustor. As in the premixed case, it is expected that in this region, the dynamics of the combustion would be determined by the competing effects of both turbulent mixing and chemical reaction, since they both are very high here. Even though the structure of this zone resembles the one observed in the premixed case, it is to be noted that the turbulent equilibrium is reached faster in the non-premixed case because of the presence of increased shear. As a result, the RMS of the axial velocity along the center line drops much more rapidly than in the premix case.

Figure 9(c) shows the contours of equivalence ratio. It can be observed that the fuel and air are thoroughly mixed, by the time the flow passes half the length of the combustor. This produces a homogeneous lean mixture similar to those observed in premixed combustion. Several interesting features can be observed in this figure. Near the tip of the injector, the stoichiometric surface (contours of $\phi = 1$ marked by near red

colors) is very thin similar to conventional burner stabilized flames. This is likely to produce a thin reaction zone with strong thermal gradients that can possibly increase the emissions. But in SPRF combustor, this situation is avoided due to the entrainment of the outflowing gases by the high velocity air. This dilutes the fuel-air mixture. As a result, within two diameters of the annular jet, the contours of $\phi = 1$ are no longer confined to a thin surface. Instead the entire combustor volume around the central region is filled with a fuel-air mixture that is lean (approximately $\phi = 0.58$). This is the primary requirement for realizing mild combustion with low emission.

Figures 10(a) and (b) compares the profiles of mean axial velocity obtained from the non-premixed simulation with the non-reactive premixed simulations. The qualitative structure of the mean axial velocity field resembles the premixed case very much. The entrainment/recirculation bubble extends only up to 200 mm (approximately), whereas in the premixed case, entrainment/recirculation zone extends up to 240 mm. This indicates that the extent of stagnation is bigger in the non-premixed case than that of the premixed case. Figures 11(a) and (b) compares the profiles of RMS of the axial velocity obtained from the the non-premixed simulation with the non-reactive premixed simulations. Again, the qualitative structure exhibits a striking similarity, even though the turbulence levels are little higher in the premixed case. The similarity in the momentum field indicates the likelihood that the scalar mixing and hence the flame structure could also be similar.

## VI. Conclusions

A combined LES / PIV technique has been used to investigate the mixing characteristics, flow and flame structures and turbulence-chemistry interactions in a Stagnation Point Reverse Flow combustor developed in Georgia Tech. Three cases have been investigated. A non-reactive flow in the premixed mode, a reactive flow in the premixed mode and a non-reactive flow in the non-premixed mode. Non-reactive LES has been compared with the corresponding PIV data. The comparison of the mean and RMS of the axial velocities shows reasonable agreement. Qualitative comparison of the flow features obtained in LES are in good agreement with the PIV. The reactive LES study uses a simple EBU model along with a four-step, eight species chemical mechanism. Increased entrainment, higher turbulent intensities and pronounced exhaust gas recirculation are observed in the reactive flow simulation. Even though the flame structure resembles a conventional flame, regions of smooth thermal gradients and weak reaction rates were also observed due to the exhaust gas entrainment and dilution. $CO$ concentration at the exhaust is over-predicted by the current EBU model, but is still qualitatively realistic. Non-premixed simulations performed in the current study uses the same flow rate and global equivalence ratio of the non-reactive flow in the premixed mode. These simulations reveal that the fuel-air mixture is thoroughly mixed in the central region of the combustor, where turbulent mixing and entrainment are high. The qualitative flow structures and the momentum field resembles the non-reactive flow in the premixed mode, indicating the possibility that the combustion performance of the SPRF combustor in non-premixed and premixed mode are comparable.

## Acknowledgments

This work is supported by the NASA's URETI (University Research Engineering Technology Institute) program.

## References

[1]Wunning, J. A. and Wunning, J. G., "Flameless oxidation to reduce thermal NO-formation," *Progress in energy and combustion science*, Vol. 29, 1997, pp. 81–94.

[2]Tsuji, H., Gupta, A., Hasegawa, T., Katsuki, M., Kishimoto, K., and Morita, M., *High Temperature Air Combustion: From Energy Conservation to Pollution Reduction*, CRC Press, 2003.

[3]Katsuki, M. and Hasegawa, T., "The science and technology of combusion in highly preheated air," *Proceedings of the*

*combustion institute*, Vol. 27, 1998, pp. 3135–3146.

[4]Sato, J., *First asia pacific conference on combustion, The Australia, New Zealand, Chinese, Taipei, Japanese and Korean Sections of the Combustion Institute*, 1997, pp. 286–289.

[5]Fujimori, T., Richelmann, D., and Sato, J., *Proceedings of the Combustion Institute*, Vol. 27, 1998, pp. 1149–1155.

[6]Neumeier, Y., Zinn, B., Weksler, Y., Seitzman, J., Jagoda, J., and Kenny, J., "Novel Combustor for Ultra Low Emissions with Non Premixed Reactants Injection," *AIAA-2005-3775, 41st AIAA Joint Propulsion Conference*, 2005.

[7]Plessing, T. Peters, N. and Wunning, J. G., "Laseroptical investigation of highly preheated combustion with strong exhaust gas recirculation," *Proceedings of the Combustion Institute*, Vol. 27, 1998, pp. 3197–3204.

[8]Fureby, C., *On Modelling of Unsteady Combustion utilizing Continuum Mechanical mixture Theories and Large Eddy Simulations*, Ph.D. thesis, Lund Institute of Technology, Sweden, 1995.

[9]Veynante, D. and Poinsot, T., "Reynolds Averaged and Large Eddy Simulation Modelling for Turbulent Combustion," *New Tools in Turbulence ModeLling*, edited by O. Metais and J. Ferziger, Springer-Les Editions De Physique, 1996.

[10]Schumann, U., "Subgrid Scale Model for Finite Difference Simulations of turbulent Flows in Plane Channels and Annuli," *Journal of Computational Physics*, Vol. 18, 1975, pp. 376–404.

[11]Menon, S., Yeung, P.-K., and Kim, W.-W., "Effect of Subgrid Models on the Computed Interscale Energy Transfer in Isotropic Turbulence," *Computers and Fluids*, Vol. 25, No. 2, 1996, pp. 165–180.

[12]Chakravarthy, V. and Menon, S., "Large-Eddy Simulations of Turbulent Premixed Flames in the Flamelet Regime," *Combustion Science and Technology*, Vol. 162, 2001, pp. 175–222.

[13]Kim, W.-W., Menon, S., and Mongia, H. C., "Large Eddy Simulations of a Gas Turbine Combustor Flow," *Combustion Science and Technology*, Vol. 143, 1999, pp. 25–62.

[14]Dimotakis, P. E., "Turbulent Free shear layer Mixing," *AIAA-89-0262*, 1989.

[15]Poinsot, T. and Veynante, D., *Theoretical and Numerical Combustion*, Edwards, Inc., 2001.

[16]Poinsot, T. and Lele, S., "Boundary Conditions for Direct Simulations of Compressible Viscous Flow," *Journal of Computational Physics*, Vol. 101, 1992, pp. 104–129.

[17]Fureby, C. and Lofstrom, C., "Large Eddy Simulation of Bluff Body Stabilized Flames," *Proceedings of the Combustion Institute*, Vol. 25, 1994, pp. 1257–1264.

[18]Peters, N. and Kee, R. J., "The computation of stretched laminar methane-air diffusion flames using a reduced four-step mechanism," *Combustion and Flame*, Vol. 68, 1987, pp. 17–29

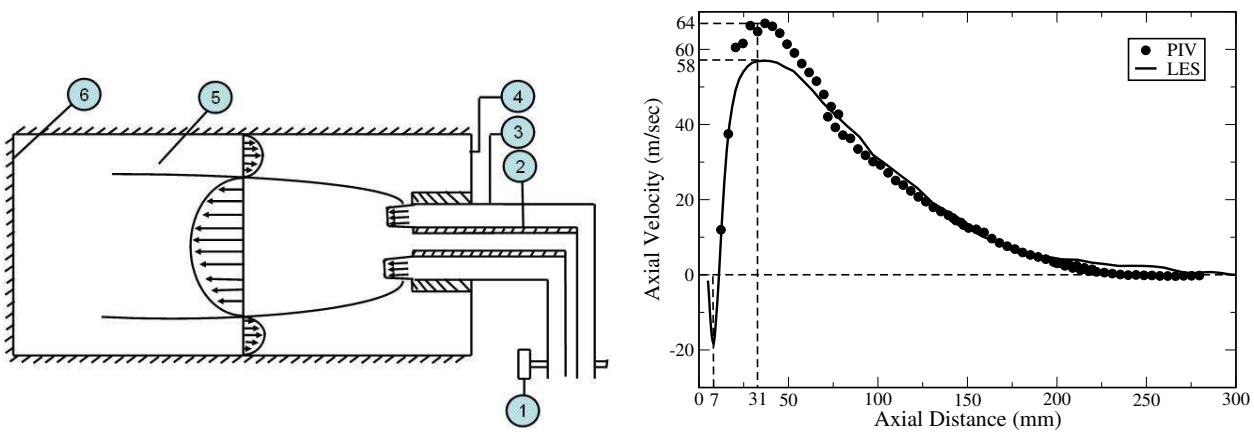


(a) Schematic diagram of the SPRF combustor

(b) Center line mean axial velocity

**Figure 1. Schematic diagram of the SPRF combustor and center-line variation of the mean axial velocity for the non-reactive premixed case**

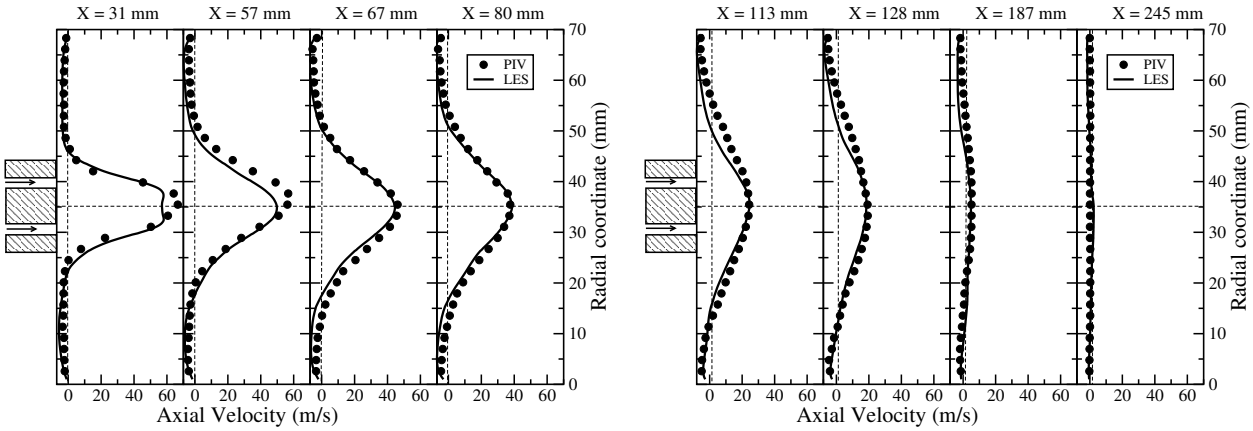


(a) Mean axial velocity

(b) Mean axial velocity

**Figure 2. Profiles of the mean axial velocity for the non-reactive premixed case**

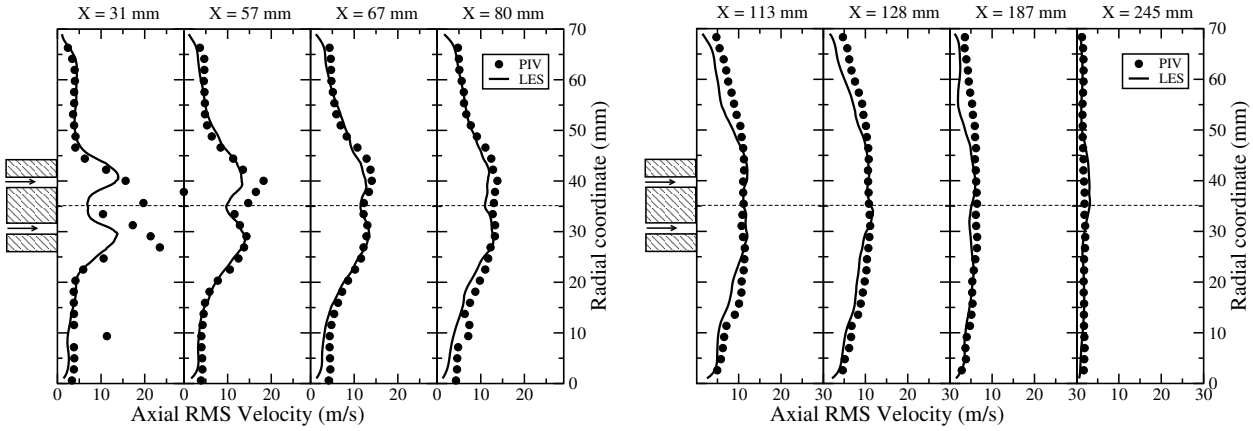


(a) RMS of axial velocity

(b) RMS of axial velocity

**Figure 3. Profiles of RMS of the axial velocity for the non-reactive premixed case**

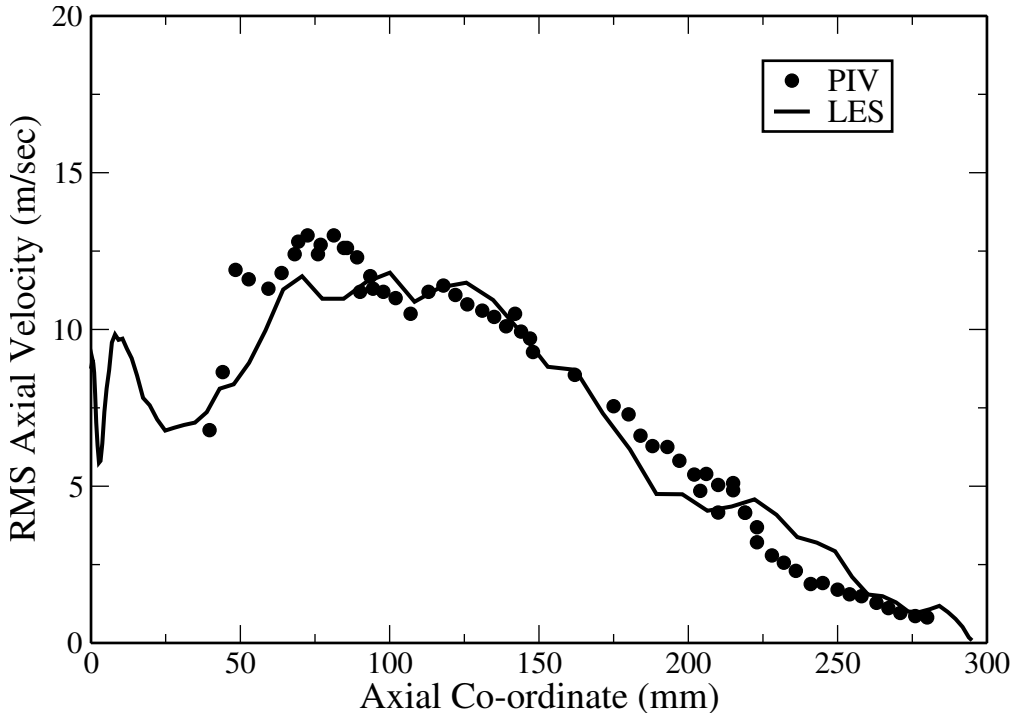


(a) RMS of axial velocity along the center-line

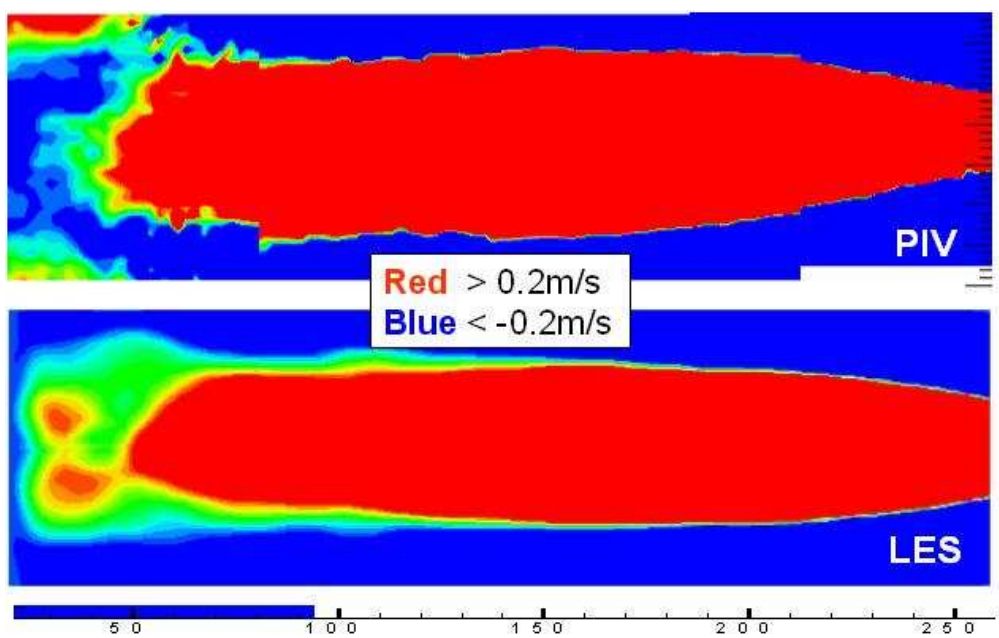


(b) Contours of axial velocity showing the zero velocity regions.

**Figure 4. Contours of mean axial velocity for the non-reactive premixed case**

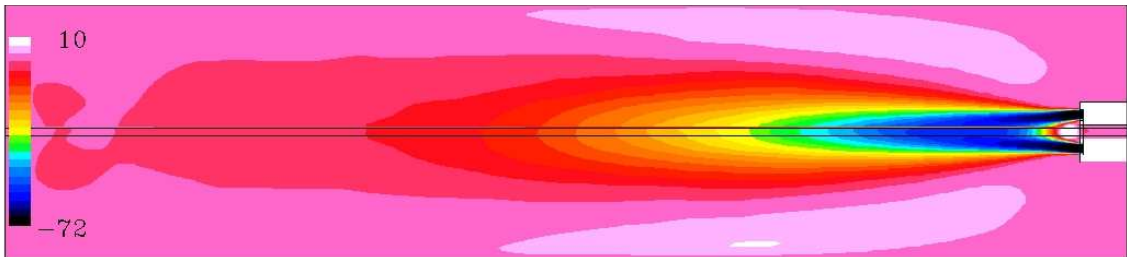


(a) Mean axial velocity contours

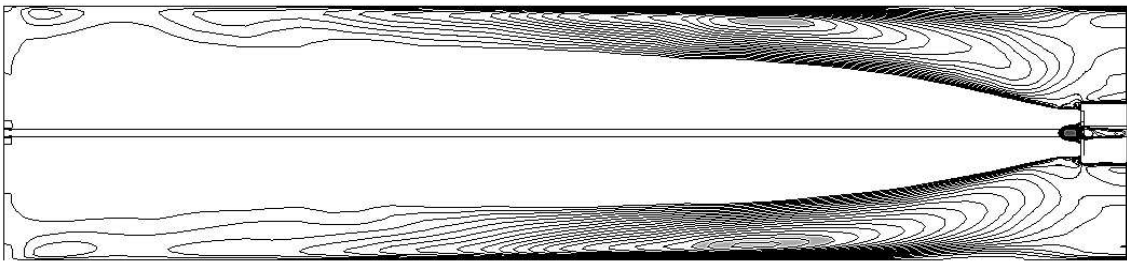

(b) Stream lines

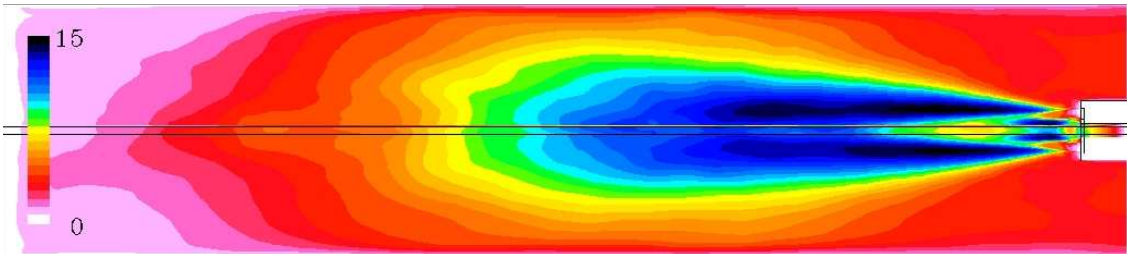


(c) RMS of the axial velocity contours

**Figure 5. Contours of mean and RMS of the axial velocity for the non-reactive premixed case**

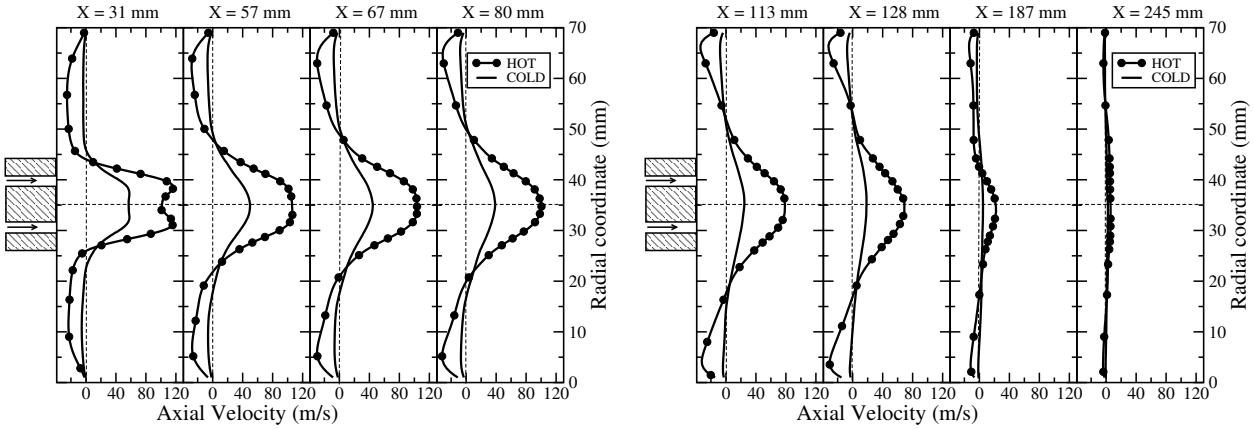


(a) Mean axial velocity profiles

(b) Mean axial velocity profiles

**Figure 6. Profiles of the mean axial velocity for the premixed combustion case**

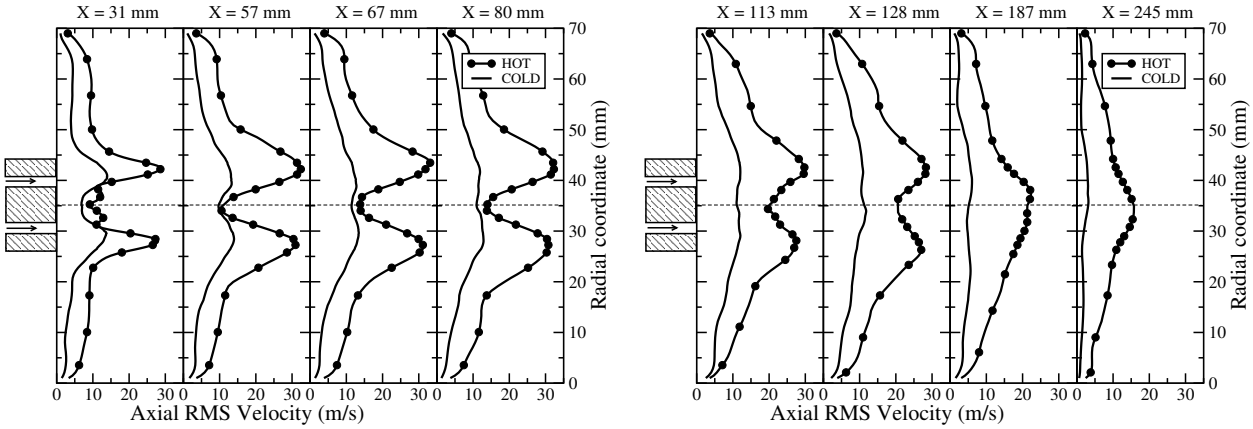


(a) Mean axial velocity

(b) Mean axial velocity

**Figure 7. Profiles of the rms of axial velocity for the premixed combustion case**

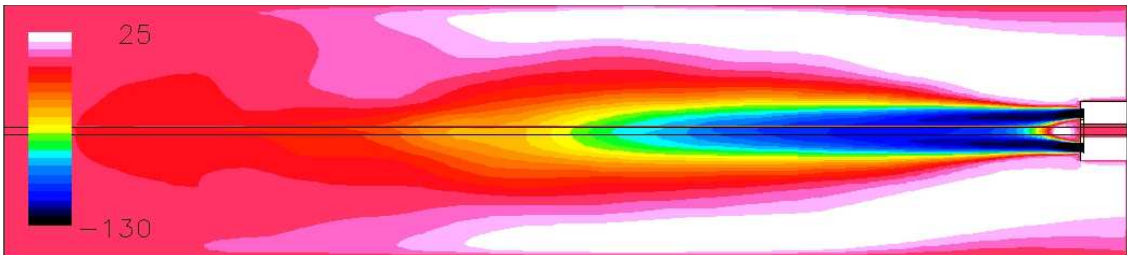


(a) Mean axial velocity contours

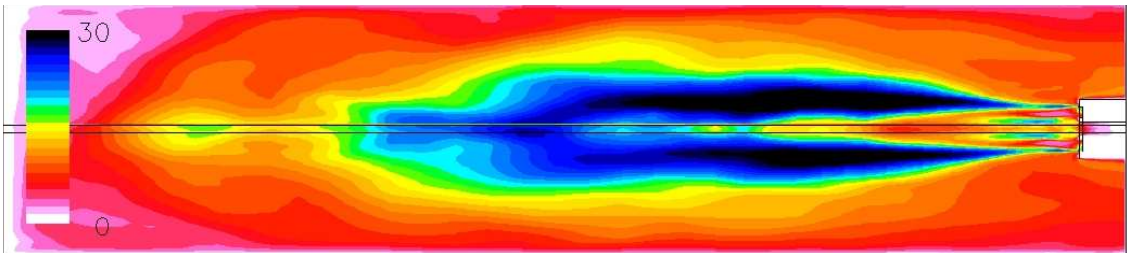


(b) RMS of axial velocity contours

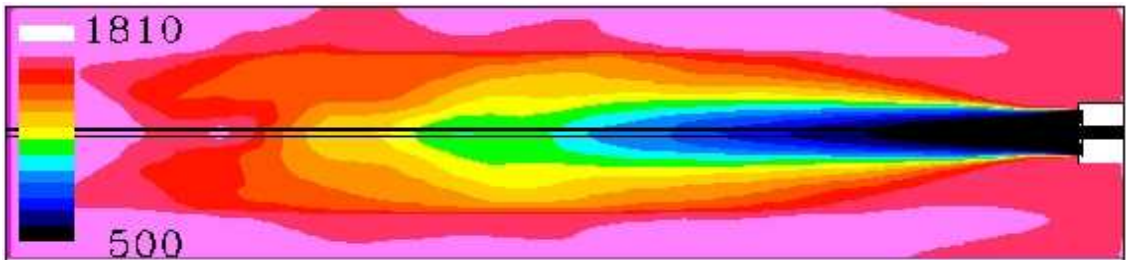


(c) Mean temperature contours

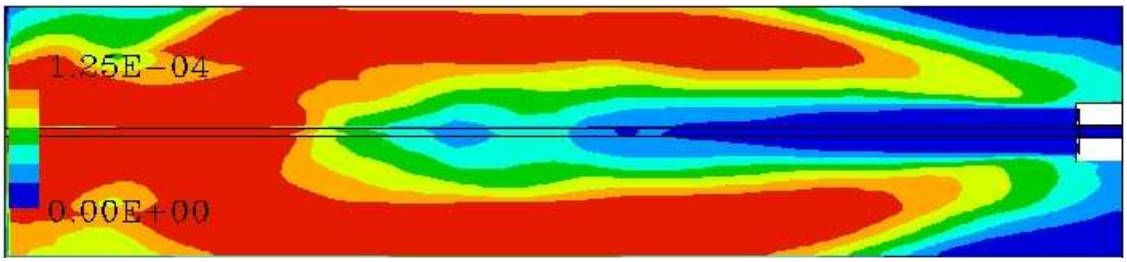


(d) Mean CO mass fraction contours

**Figure 8. Contours of mean and RMS axial velocity, temperature and CO mass fraction for the premixed combustion case**

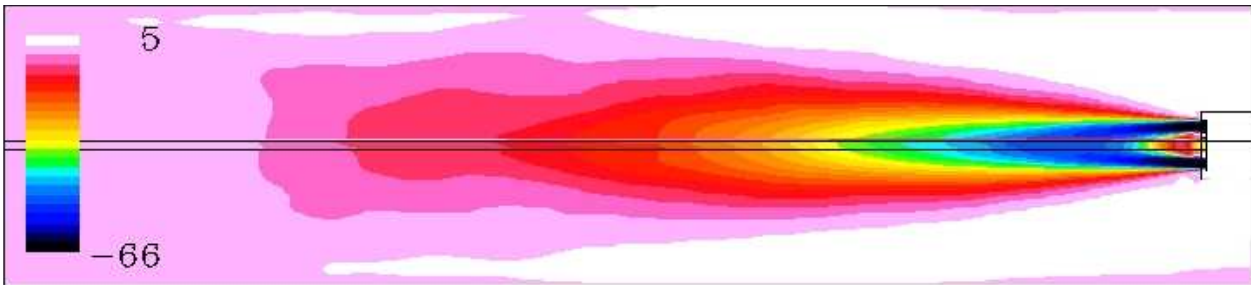


(a) Mean axial velocity contours

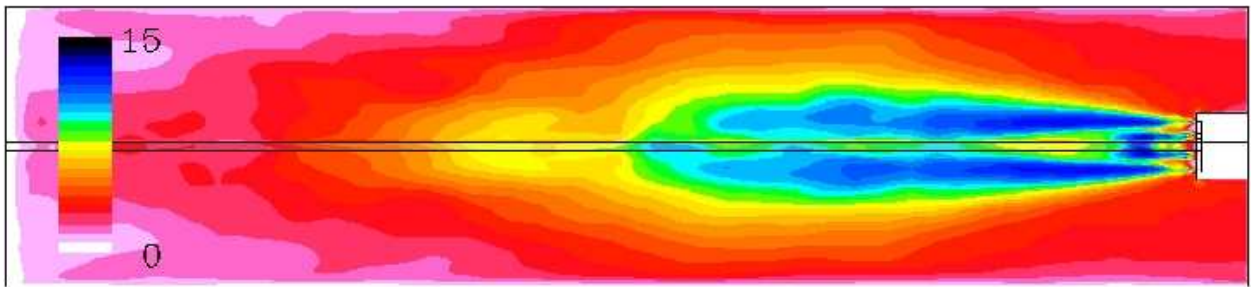


(b) RMS of the axial velocity contours

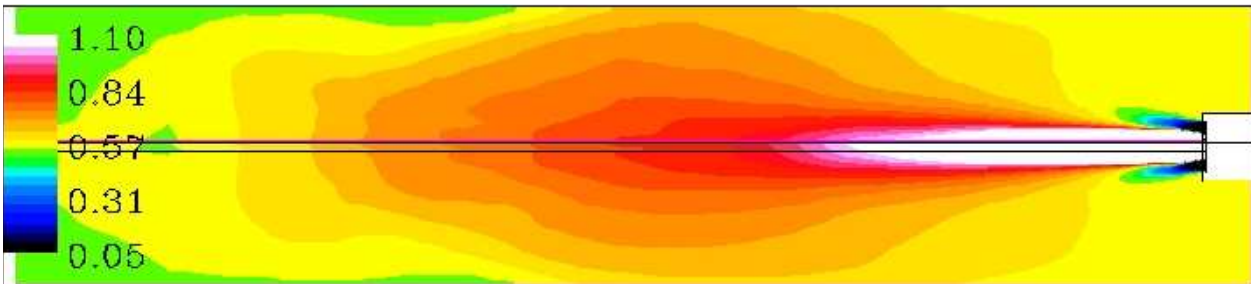


(c) Mean equivalence ratio contours

**Figure 9. Contours of Mean Axial velocity, RMS of axial velocity and mean equivalence ratio for the non-premixed scalar mixing case**

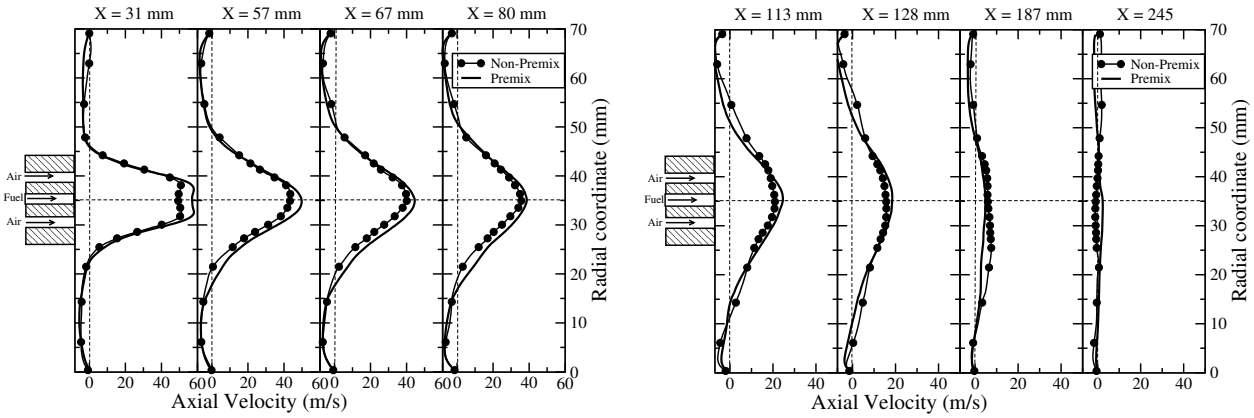


(a) Mean axial velocity profiles

(b) Mean axial velocity profiles

**Figure 10. Profiles of mean axial velocity for the non-premixed scalar mixing case**

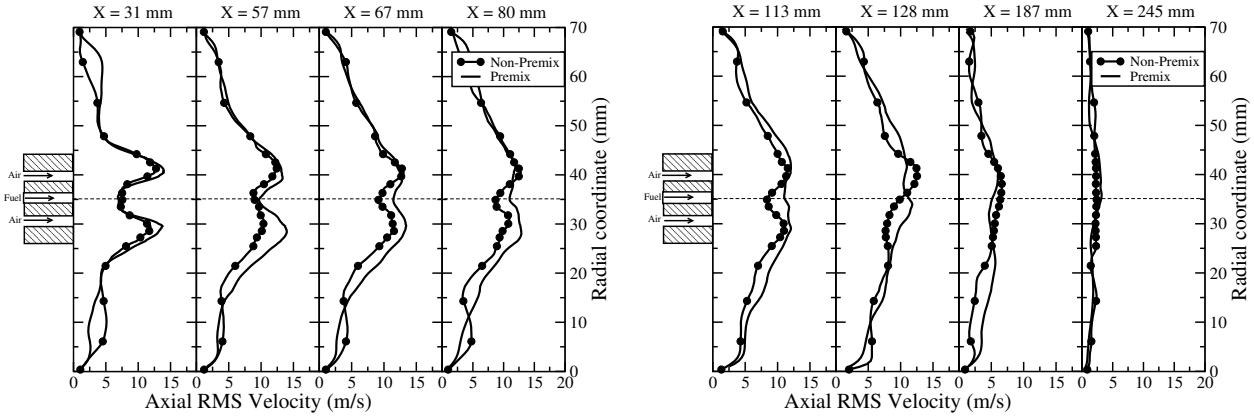


(a) RMS of axial velocity profiles

(b) RMS of axial velocity profiles

**Figure 11. Profiles of RMS of the axial velocity for the non-premixed scalar mixing case**